IEEE Access
Multidisciplinary | Rapid Review | Open Access Journal

Received October 6, 2021, accepted November 2, 2021, date of publication November 10, 2021,
date of current version November 22, 2021.

Digital Object Identifier 10.1109/ACCESS.2021.3127206

Spectral Element Method for the Elastic/Acoustic Waveguide Problem in Anisotropic Metamaterials

AN QI GE[1,2], MING WEI ZHUANG[2], (Member, IEEE), JIE LIU[2,3], (Member, IEEE), AND QING HUO LIU[4], (Fellow, IEEE)

[1]School of Mathematical Sciences, Xiamen University, Xiamen 361005, China
[2]Institute of Electromagnetics and Acoustics and Key Laboratory of Electromagnetic Wave Science and Detection Technology, Xiamen University, Xiamen 361005, China
[3]Postdoctoral Mobile Station of Information and Communication Engineering, School of Informatics, and Institute of Electromagnetics and Acoustics, Xiamen University, Xiamen 361005, China
[4]Department of Electrical and Computer Engineering, Duke University, Durham, NC 27708, USA

Corresponding authors: Qing Huo Liu (qhliu@duke.edu) and Jie Liu (liujie190484@163.com)

This work was supported in part by the National Key Research and Development Program of China under Grant 2018YFC0603503, and in part by the China Postdoctoral Science Foundation under Grant 2019M662244.

ABSTRACT Waveguide problems are fundamental to elastic and acoustic wave propagation, where we are interested in finding the propagation constants and modal patterns of waveguide modes. As the waveguide is assumed uniform in one direction, the original 3-D problem can be converted into a so-called 2.5-D problem by using the Fourier transform in that direction. However, the introduction of elastic metamaterials (EMM) broadens the horizon of this subject, and new features are required in EMM waveguides that cannot be obtained by most traditional waveguide solvers. In this work, a spectral element method (SEM) is developed to simulate the elastic/acoustic waveguide problem in anisotropic media with anisotropic mass density and/or negative index parameters. We design an anisotropic density EMM waveguide with our SEM solver to demonstrate several intriguing phenomena. Comparisons with the traditional finite element method (FEM) for several examples show the significant advantages of the SEM in term of accuracy and efficiency.

INDEX TERMS Elastic waveguide, spectral element method, metamaterials, anisotropic density media.

I. INTRODUCTION

Recently, elastic waveguide problems have gained much attention due to various engineering applications, for example, ultrasound characterization, non-destructive testing, and structural health monitoring [1]–[3]. For various types of elastic waveguides [4], the mode analysis [5], [6] is an important research topic, because wave propagation and scattering phenomena in a waveguide can be described as the superposition of all of the propagation modes and evanescent modes. In this class of problems, one is interested in solving the propagation constants and the corresponding field distributions of individual modes in a given waveguide structure.

As an extension of the electromagnetic and acoustic waveguides [7]–[9], Lagasse proposes a finite element method (FEM) for computing the eigenmodes of the homogeneous elastic waveguides of arbitrary cross sections [10]; Kosmodamianskii *et. al.* derive the equation for normal elastic waves in a longitudinally anisotropic cylindrical waveguide with a circular cross-section [11]; and Gravenkamp *et. al.* develop the scaled boundary finite element method (SBFEM) for an inhomogeneous isotropic elastic waveguide [12]. A semi-analytical finite element method (SAFEM) has been developed to simulate the solid-fluid coupling waveguide [13]–[15] and an open waveguide with the absorbing boundary condition [16]. Moreover, the spectral element method (SEM) is also used to solve the piezoelectric waveguide problem [17]. All of these investigations focus on specific problems with significant applications.

Recently, with the advent of elastic metamaterials (EMM), various new and intriguing wave propagation phenomena can be generated in such novel synthetic materials [18]–[21]. As EMMs can involve negative refractive index materials and/or anisotropic mass density, most traditional numerical waveguide solvers such as the finite difference (FD) method [22], FEM [23]–[25] and SEM [17], [26] have not been modified to accommodate the modeling of such EMM waveguides.

In recent years, the SEM has been successfully developed for analyzing the propagation and scattering of elastic waves [27]–[30], acoustic waves [31], [32], and electromagnetic waves [33], [34]. As a special version of the

The associate editor coordinating the review of this manuscript and approving it for publication was Zhongyi Guo.

high-order FEM, the SEM not only takes advantage of the geometric flexibility of the FEM, but also has the high accuracy of spectral methods. Moreover, the use of the Gauss-Lobatto-Legendre (GLL) polynomials for the nodal basis functions makes the numerical error converges exponentially with the order of basis functions. Therefore, at the same accuracy requirement, the SEM requires much fewer degrees of freedom (DOFs) than the FEM, so it can save huge computational costs.

This investigation aims at developing an effective SEM for an inhomogeneous elastic waveguide of an arbitrary cross section applicable to both anisotropic solid materials and all kinds of EMMs, for instance, negative index, anisotropic mass density and so on, for the first time. In addition, the waveguide system with both solids and fluids is also treated by considering the fluid-solid coupling. The external boundary of the waveguide cross section can allow different boundary conditions based on the given general formulations of the boundary terms, for example, the hard boundary condition, the soft boundary condition, the Bloch periodic boundary condition and the absorbing boundary condition for an unbounded (open) waveguide. Numerical examples show the significant advantages of the SEM in term of accuracy and computation efficiency compared with the conventional FEM as implemented by COMSOL. We also investigate waveguides with anisotropic density that cannot be solved by commercial solvers.

The organization of this paper is as follows. In Section II, we will present the detailed weak formulation of the elastic waveguide. The discretization by the SEM is shown in Section III. Finally, the accuracy and efficiency of the SEM are demonstrated by several examples in Section IV.

II. GOVERNING EQUATIONS AND WEAK FORMULATIONS

A. GOVERNING EQUATIONS

For a general anisotropic and inhomogeneous elastic metamaterial with a potentially anisotropic mass density, elastic wave equations in frequency domain read

$$\begin{cases} \boldsymbol{\rho}\omega^2 \cdot \boldsymbol{u} + \boldsymbol{\nabla} \cdot \boldsymbol{\tau} = \mathbf{0} & \text{(1a)} \\ \boldsymbol{\tau} = \boldsymbol{c} : \boldsymbol{\epsilon} & \text{(1b)} \\ \boldsymbol{\epsilon} = (\boldsymbol{\nabla}\boldsymbol{u} + \boldsymbol{\nabla}\boldsymbol{u}^T)/2 & \text{(1c)} \end{cases}$$

where $\boldsymbol{\rho} = (\rho_{ij})_{3\times3}$ is the anisotropic mass density; ω denotes the angular frequency, $\boldsymbol{u}$ is the particle displacement; $\boldsymbol{\epsilon}$, $\boldsymbol{\tau}$ are the 2nd-order strain and stress tensors; $\boldsymbol{c}$ is the 4th-order elastic tensor. In Voigt notation, c_{ijkl} can be converted to a second-order tensor $(C_{rs})_{6\times6}$. The subscripts of $\boldsymbol{C}$ and $\boldsymbol{c}$ satisfy the relations between (r, s) and (i, j, k, l): $1 \leftrightarrow 11$, $2 \leftrightarrow 22$, $3 \leftrightarrow 33$, $4 \leftrightarrow 23$, $5 \leftrightarrow 13$ and $6 \leftrightarrow 12$. Therefore, the constitutive equation (1b) can be transformed into a matrix form [35]. And the divergence of $\boldsymbol{\tau}$ computed by the left divergence operator can be expressed as

$$\nabla \cdot \boldsymbol{\tau} = \hat{\mathbf{e}}_k \partial x_k \cdot \tau_{ji}\hat{\mathbf{e}}_j \otimes \hat{\mathbf{e}}_i = \sum_{j=1}^{3} \frac{\partial \tau_{ji}}{\partial x_j}\hat{\mathbf{e}}_i \triangleq \tau_{ji,j}\hat{\mathbf{e}}_i \qquad (2)$$

where Einstein's convention has been adapted, with the repeated indices implying summation. The operators "$\otimes$" and "$\cdot$" represent the diadic product and the dot product, respectively. Substituting (2) into (1a) yields

$$\omega^2 \rho_{ij} u_j(x, y, z) + \tau_{ji,j} = 0 \qquad (3)$$

The Latin subscripts $i, j, k, \ldots$ represent three-dimensional indices and the Greek subscripts $\alpha, \beta, \ldots$ are two-dimensional indices. It is well known that the waveguide problem is actually a 2.5-dimensional problem, where the field is three-dimensional depending on $(x_1, x_2, x_3) = (x, y, z)$ but the materials are two-dimensional depending on (x_1, x_2). When the propagation is along the $+z$-axis and the cross section of the waveguide is uniform in the z-direction, the phasor expression for displacement field $\boldsymbol{u}$ and the operator $\boldsymbol{\nabla}$ can be written explicitly as

$$\boldsymbol{u} = \hat{\mathbf{e}}_i u_i(x, y) e^{-\gamma_z z} e^{\mathrm{j}\omega t} \qquad \text{(4a)}$$

$$\boldsymbol{\nabla} = \hat{\mathbf{e}}_1 \frac{\partial}{\partial x_1} + \hat{\mathbf{e}}_2 \frac{\partial}{\partial x_2} - \hat{\mathbf{e}}_3 \mathrm{j}\mathrm{k}_z \equiv \boldsymbol{\nabla}_t - \hat{\mathbf{e}}_3 \gamma_z \qquad \text{(4b)}$$

for any given waveguide mode, where $\hat{\mathbf{e}}_i$ and $u_i(x, y)$ denote the i-th unit vector and its corresponding component of the displacement field in Cartesian coordinates, respectively, and $\gamma_z = \mathrm{j}\mathrm{k}_z = \alpha_z + \mathrm{j}\beta_z$ is the complex propagation constant (the real variables α_z and β_z are called the attenuation constant and phase constant respectively). k_z is the z-component of the wave vector. In the following formulations, the time convention $e^{\mathrm{j}\omega t}$ is omitted. Therefore, substituting (4) into (1c), the strain tensor can be written as

$$\boldsymbol{\epsilon} = e^{-\gamma_z z} \begin{bmatrix} u_{1,1} & \frac{u_{1,2}+u_{2,1}}{2} & \frac{u_{3,1}-\gamma_z u_1}{2} \\ \frac{u_{1,2}+u_{2,1}}{2} & u_{2,2} & \frac{u_{3,2}-\gamma_z u_2}{2} \\ \frac{u_{3,1}-\gamma_z u_1}{2} & \frac{u_{3,2}-\gamma_z u_2}{2} & -\gamma_z u_3 \end{bmatrix} \qquad (5)$$

On the other hand, the stress tensor can be expressed as $\boldsymbol{\tau} = e^{-\gamma_z z}\tau_{ij}\hat{\mathbf{e}}_i \otimes \hat{\mathbf{e}}_j$, and the components τ_{ij} are indicated as

$$\tau_{ij} = C_{r(i,j),r(k,\alpha)} u_{k,\alpha} - \gamma_z C_{r(i,j),r(k,3)} u_k \qquad (6)$$

where the subscripts of C come from the elements of a symmetrical constant matrix r defined by

$$r = \begin{bmatrix} 1 & 6 & 5 \\ 6 & 2 & 4 \\ 5 & 4 & 3 \end{bmatrix}$$

Obviously, $\boldsymbol{\tau}$ is also symmetrical. Inserting (4)-(6) into (3), we can obtain the governing equation of the elastic waveguide as follows

- Component formulation:

$$\gamma_z^2 \ell_{3ij3} u_j - \gamma_z [\partial x_\alpha (\ell_{\alpha ij3} u_j) + \ell_{3ij\alpha} u_{j,\alpha}] + \partial x_\alpha (\ell_{\alpha ij\beta} u_{j,\beta}) + \omega^2 \rho_{ij} u_j = 0 \qquad (7)$$

- The components of the coefficient tensor $\boldsymbol{\ell} = \ell_{kijm}\hat{\mathbf{e}}_k \otimes \hat{\mathbf{e}}_i \otimes \hat{\mathbf{e}}_j \otimes \hat{\mathbf{e}}_m$ are denoted by

$$\ell_{kijm} = C_{r(i,k),r(j,m)} \qquad (8)$$

It is easy to see that (7) is a quadratic eigenvalue problem, where $\gamma_z = \mathrm{j}k_z = \alpha_z + \mathrm{j}\beta_z$ is the eigenvalue and $\boldsymbol{u}$ denotes the corresponding eigenvector. The goal of this work is to develop the SEM for solving the eigenpairs $(\gamma_z, \boldsymbol{u})$.

B. WEAK FORMULATION

Based on the framework of FEM, multiplying equation (7) by the test function φ and integrating and using the integration by parts for the second and fourth integrations, we arrive at the weak form equation for the solid region

$$\gamma_z^2 a_{ij}(u_j, \varphi) - \gamma_z[b_{ij}(u_j, \varphi) + I_1] + q_{ij}(u_j, \varphi) + I_2 = 0 \quad (9)$$

The above bilinear functions can be written in detail as

$$\begin{aligned}
a_{ij}(u_j, \varphi) &= \int_\Gamma \varphi^\dagger(\ell_{3ij3}u_j)dxdy \\
b_{ij}(u_j, \varphi) &= \int_\Gamma \varphi^\dagger(\ell_{3ij\alpha}u_{j,\alpha})dxdy \\
&\quad - \int_\Gamma (\partial x_\alpha \varphi)^\dagger(\ell_{\alpha ij3}u_j)dxdy \\
q_{ij}(u_j, \varphi) &= \int_\Gamma \omega^2\varphi^\dagger(\rho_{ij}u_j)dxdy \\
&\quad - \int_\Gamma (\partial x_\alpha \varphi)^\dagger(\ell_{\alpha ij\beta}u_{j,\beta})dxdy \\
I_1 &= \int_{\partial\Gamma} \varphi^\dagger(n_\alpha \ell_{\alpha ij3}u_j)dx \\
I_2 &= \int_{\partial\Gamma} \varphi^\dagger(n_\alpha \ell_{\alpha ij\beta}u_{j,\beta})dx
\end{aligned} \quad (10)$$

where Γ is the waveguide cross section; $\partial\Gamma$ denotes the boundary of Γ; $\hat{\mathbf{n}} = n_\alpha \hat{\mathbf{e}}_\alpha$ represents the unit outward normal vector at the point on the edge $\partial\Gamma$; the superscript "†" denotes the complex conjugate. Because of the existence of boundary integral items I_1 and I_2, we need one or the combination of the following boundary conditions.

C. BOUNDARY CONDITIONS

In order to solve the propagation constant γ_z within a given waveguide, for the external boundary integral $-\gamma_z I_1 + I_2$, we need the suitable boundary conditions, such as the hard boundary condition, the soft boundary condition, the Bloch periodic boundary condition and the absorbing boundary condition.

1) Hard boundary condition reads $\boldsymbol{u} = 0$. Therefore $-\gamma_z I_1 + I_2 = 0$ and the region of the integration Γ is replaced by $\Gamma \backslash \partial\Gamma$.
2) Soft boundary condition reads $\hat{\mathbf{n}} \cdot \boldsymbol{\tau} = 0$. According to (6), we have

$$n_\alpha \tau_{\alpha i} = n_\alpha[-\gamma_z(\ell_{\alpha ij3}u_j) + \ell_{\alpha ij\beta}u_{j,\beta}] \quad (11)$$

Substituting (11) into the external boundary integral, we have $-\gamma_z I_1 + I_2 = \int_{\partial\Gamma} \hat{\mathbf{n}} \cdot \boldsymbol{\tau} dx$ in view of $\hat{\mathbf{n}} \cdot \boldsymbol{\tau} = n_j \tau_{ji}$ and $n_3 = 0$ in the waveguide problem. Therefore, the boundary integrals vanish and the region of the integration is unchanged.

3) By the Bloch theorem [36], we first obtain

$$u_j(\mathbf{k}_t, \boldsymbol{r} + \boldsymbol{a}) = u_j(\mathbf{k}_t, \boldsymbol{r})e^{-\mathrm{j}\mathbf{k}_t \cdot \boldsymbol{a}} \quad (12)$$

where $\mathbf{k} = \mathbf{k}_t + \hat{z}\mathrm{k}_z$ is the Bloch wave vector, $\boldsymbol{r}$ and $\boldsymbol{a}$ are the position vectors on the boundary $\partial\Gamma$ and the lattice translation vector, respectively. Define the Bloch periodic subspace $H_p^B(\Gamma) = \{v \in H^1(\Gamma) : v(\boldsymbol{r} + \boldsymbol{a}) = v(\boldsymbol{r})e^{-\mathrm{j}\mathbf{k}_t \cdot \boldsymbol{a}} \text{ on } \partial\Gamma\}$, where $H^1(\Gamma) = \{v \in L_2(\Gamma) : \boldsymbol{\nabla}_t v \in L_2(\Gamma)^2\}$. For any φ, u_j belonging to H_p^B, from I_1 and I_2 in (10), note that the normal vectors defined on a pair of periodic boundary have opposite directions, we can obtain the external boundary integral $I_1 = I_2 = 0$. Consequently, the external boundary integrations vanish for all the opposite boundaries (BPBC) by using the Bloch periodic boundary condition on the external boundary. Meanwhile, the Bloch periodic boundary condition waveguide problem can be transformed into the following equivalent waveguide problem with purely periodic boundary conditions. When u_j are written as the plane wave form $u_j(\mathbf{k}_t, \boldsymbol{r}) = \widetilde{u}_j(\mathbf{k}_t, \boldsymbol{r})e^{-\mathrm{j}\mathbf{k}_t \cdot \boldsymbol{r}}$, we can obtain the periodic boundary conditions $\widetilde{u}_j(\mathbf{k}_t, \boldsymbol{r} + \boldsymbol{a}) = \widetilde{u}_j(\mathbf{k}_t, \boldsymbol{r})$ arising from (12). Therefore, the corresponding periodic subspace can be defined by

$$H_p(\Gamma) = \{v \in H^1(\Gamma) : v(\boldsymbol{r} + \boldsymbol{a}) = v(\boldsymbol{r}) \text{ on } \partial\Gamma\} \quad (13)$$

For any φ, u_j belonging to H_p, it is easy to check that the external boundary integrals are still zero. By replacing the operator $\boldsymbol{\nabla}_t$ with $\boldsymbol{\nabla}_t - \mathrm{j}\mathbf{k}_t$ in (9), we arrive at a new scheme

$$\gamma_z^2 \widetilde{a}_{ij}(\widetilde{u}_j, \varphi) - \gamma_z \widetilde{b}_{ij}(\widetilde{u}_j, \varphi) + \widetilde{q}_{ij}(\widetilde{u}_j, \varphi) = 0 \quad (14)$$

where the bilinear functions can be written as

$$\begin{aligned}
\widetilde{a}_{ij}(\widetilde{u}_j, \varphi) &= \int_\Gamma \varphi^\dagger(\ell_{3ij3}\widetilde{u}_j)dxdy \\
\widetilde{b}_{ij}(\widetilde{u}_j, \varphi) &= \int_\Gamma \varphi^\dagger[\ell_{3ij\alpha}(\widetilde{u}_{j,\alpha} - \mathrm{j}\mathrm{k}_\alpha \widetilde{u}_j)]dxdy \\
&\quad - \int_\Gamma (\partial x_\alpha \varphi - \mathrm{j}\mathrm{k}_\alpha)^\dagger(\ell_{\alpha ij3}\widetilde{u}_j)dxdy \\
\widetilde{q}_{ij}(\widetilde{u}_j, \varphi) &= \int_\Gamma \omega^2\varphi^\dagger \rho_{ij}\widetilde{u}_j dxdy \\
&\quad - \int_\Gamma (\partial x_\alpha \varphi - \mathrm{j}\mathrm{k}_\alpha)^\dagger[\ell_{\alpha ij\beta}(\widetilde{u}_{j,\beta} - \mathrm{j}\mathrm{k}_\beta \widetilde{u}_j)]dxdy
\end{aligned} \quad (15)$$

4) In our work, the absorbing boundary condition is used to truncate the infinite external boundary when the waveguide is unbounded in the transverse directions. From [28], the absorbing boundary condition for the scalar mass density is expressed as

$$\boldsymbol{t} = C_L \rho(\boldsymbol{v} \cdot \hat{\mathbf{n}})\hat{\mathbf{n}} + C_T \rho(\boldsymbol{v} - (\boldsymbol{v} \cdot \hat{\mathbf{n}})\hat{\mathbf{n}}) \quad (16)$$

where $\boldsymbol{t}$ is the boundary traction, $\boldsymbol{v}$ is the velocity field on the surface, and C_L, C_T represent the material bulk speed of longitudinal and transverse waves in the background outside the computational

region Γ, respectively. However, in this work we treat anisotropic density, so the boundary function is rewritten as

$$\hat{\mathbf{n}} \cdot \boldsymbol{\tau} = \mathrm{j}\omega \boldsymbol{\rho} \cdot [C_T \boldsymbol{u} + (C_L - C_T)(n_j u_j)\hat{\mathbf{n}}] \quad (17)$$

Accordingly, the scalar expressions with the Einstein notation are written as

$$\mathrm{n}_j \tau_{ji} = \mathrm{j}\omega \rho_{ij}[C_T u_j + (C_L - C_T)(\mathrm{n}_1 u_1 + \mathrm{n}_2 u_2)\mathrm{n}_j] \quad (18)$$

Moreover, noting that $\mathrm{n}_3 = 0$, the external boundary integrations in (9) are replaced by

$$-\gamma_z I_1 + I_2 = d_{ij}(u_j, \varphi) \quad (19)$$

The above bilinear function can be written in detail as

$$d_{ij}(u_j, \varphi) = \mathrm{j}\omega \int_{\partial\Gamma_{\mathrm{ext}}} \varphi^\dagger [\rho_{ij} C_T + (C_L - C_T)\mathrm{n}_j \rho_{i\alpha} \mathrm{n}_\alpha] u_j dx \quad (20)$$

The weak formulations of the elastic waveguide for the pure solid model with the Bloch periodic boundary condition and the absorbing boundary condition are expressed compactly as

$$\gamma_z^2 a_{ij}(u_j, \varphi) - \gamma_z b_{ij}(u_j, \varphi) + q_{ij}(u_j, \varphi) + I_3 = 0 \quad (21a)$$

$$I_3 = \begin{cases} 0 & \text{for Hard, Soft and BPBC} \\ d_{ij}(u_j, \varphi) & \text{for ABC} \end{cases} \quad (21b)$$

The above is for the case where all materials are solid in the waveguide. If part of the waveguide is made of fluid, we need to consider the special coupling between fluid and solid in the eigenvalue problem.

D. THE FLUID-SOLID COUPLING SYSTEM

When the waveguide is filled with an inhomogeneous medium including parts of fluid and solid, we need to consider the fluid-solid coupling. The symbol "f" is introduced to denote the local fluid region f, which shares the common interface $\partial\Gamma_{fs}$ with the local solid region s shown in Fig 1. For the fluid-solid coupling system, we not only derive the weak form in the fluid region, but also give the continuity condition of the fluid-solid at the interface defined by $\partial\Gamma_{fs}$. First, the governing equation for the potential χ, defined as $\boldsymbol{v} = \rho_f^{-1} \boldsymbol{\nabla} \chi$, in the fluid region is introduced from [29]

$$\boldsymbol{\nabla} \cdot (\rho_f^{-1} \boldsymbol{\nabla} \chi) + \kappa^{-1} \omega^2 \chi = 0 \quad (22)$$

where ρ_f is the density of fluid/acoustic materials and κ is the bulk modulus. The phasor expression for potential is shown as $\chi = \chi(x, y)e^{-\gamma_z z}$. Multiplying (22) by the test function ψ and integrating, after using the integration by parts, we obtain the weak form for the fluid region

$$\gamma_z^2 e(\chi, \psi) - f(\chi, \psi) + I_4 = 0 \quad (23)$$

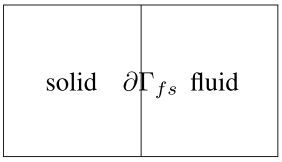

FIGURE 1. The solid region s (left) and the fluid region f (right) with an interface $\partial\Gamma_{fs}$.

The above bilinear functions can be expressed as follows

$$\begin{aligned} e(\chi, \psi) &= \int_\Gamma \psi^\dagger \rho_f^{-1} \chi \, dxdy \\ f(\chi, \psi) &= \int_\Gamma (\partial_\alpha \psi)^\dagger (\rho_f^{-1} \partial_\alpha \chi) - \psi^\dagger \kappa^{-1} \omega^2 \chi \, dxdy \\ I_4 &= \int_{\partial\Gamma} \psi^\dagger (n_\alpha \rho_f^{-1} \partial_\alpha \chi) dx \end{aligned} \quad (24)$$

Second, when the boundary integral $-\gamma_z I_1 + I_2$ in (9) is restricted to the interface $\partial\Gamma_{fs}$ between the solid region and the fluid region, because of the continuity condition of the traction $\hat{\mathbf{n}} \cdot \boldsymbol{\tau} = \mathrm{j}\omega\chi\hat{\mathbf{n}}$ [29] and the fact $\mathrm{n}_3 = 0$, it follows that

$$-\gamma_z I_1^{fs} + I_2^{fs} = \int_{\partial\Gamma_{fs}} \varphi^\dagger \mathrm{j}\omega \chi(x, y)\mathrm{n}_i dx \triangleq I_5^{fs} \quad (25)$$

Finally, for the fluid region, similarly, the external boundary integration I_4 satisfies

$$I_4 = \begin{cases} 0, & \text{for Hard, Soft, and BPBC} \\ \mathrm{j}\omega \int_{\partial\Gamma_{\mathrm{ext}}} \psi^\dagger (\rho_f C_L)^{-1} \chi \, dx, & \text{for ABC} \end{cases} \quad (26)$$

On the other hand, by replacing the normal component of the velocity $\hat{\mathbf{n}} \cdot \boldsymbol{v}_{\mathrm{fluid}} = \hat{\mathbf{n}} \cdot (\rho_f^{-1} \nabla \chi)$ in the fluid region with the normal component of the velocity $\hat{\mathbf{n}} \cdot (\mathrm{j}\omega \boldsymbol{u})$ in the solid region [29], I_4^{fs} can be derived as

$$I_4^{fs} = \mathrm{j}\omega \int_{\partial\Gamma_{fs}} \psi^\dagger \mathrm{n}_j u_j dx \quad (27)$$

Compactly, the weak formulations of the fluid-solid coupling system are shown as (28), as shown at the bottom of the next page.

Note that, when the cladding medium outside a core of the waveguide is filled with solid, $-\gamma_z I_1 + I_2$ is replaced by I_3 shown in (21b) and $I_4 = 0$. Conversely, when the cladding is a fluid region, $-\gamma_z I_1 + I_2 = 0$ and I_4 is shown in (26).

The above completes the formulation of elastic waveguide and its weak formulations. In the next section, we will introduce the discretization scheme to calculate the propagation constants γ_z of the waveguide and their corresponding modes (eigenvectors).

III. BASIS FUNCTIONS AND DISCRETIZATION

A. BASIS FUNCTIONS

In order to approximate the unknown field component u_j, we apply the Gauss-Lobatto-Legendre (GLL) polynomials as the basis functions. The Nth-order 1D GLL polynomials are defined as

$$\phi_r^{(N)} = \frac{-1}{N(N+1)L_N(\xi_r)} \frac{(1-\xi^2)L_N'(\xi)}{(\xi-\xi_r)}, \quad r \in \mathbb{N}^+ \tag{29}$$

where the interpolating points $\xi_r \in [-1, 1]$, and they are chosen as the GLL points which are the roots of equation $(1-\xi_r^2)L_N'(\xi_r) = 0$, and $L_N'(\xi)$ is the derivative of the Nth-order Legendre polynomial. Note that, the Legendre polynomials are orthogonal polynomials that allow to reduce the interpolation errors compared to the standard Lagrange polynomials used in the FEM. u_j can be approximated by using the tensor-product $\varphi_p^{(N)} = \phi_r^{(N)}(\xi)\phi_s^{(N)}(\eta)$ of two 1D nodal basis functions, where the subscript p is the compound index of (r, s). Let the physical domain be subdivided into a number of non-overlapping quadrilateral elements, so that each element can be mapped into the reference element $[-1, 1] \times [-1, 1]$ by the mapping $x(\xi, \eta), y(\xi, \eta)$ [7], [37]. For example, the irregular element κ with curved edges can be mapped to the reference element $\hat{\kappa}$ by using the curvilinear mapping shown in Fig 2. While the corresponding invertible mappings are applied to the basis function $\varphi(x, y) = \widehat{\varphi}(\xi, \eta)$ and $\nabla_t \varphi(x, y) = \mathbf{J}^{-1}\widehat{\nabla}_t \widehat{\varphi}(\xi, \eta) \triangleq \mathcal{J}_\alpha \hat{\varphi} \hat{\mathbf{e}}_\alpha$, where $\mathbf{J} = \begin{bmatrix} \frac{\partial x}{\partial \xi} & \frac{\partial y}{\partial \xi} \\ \frac{\partial x}{\partial \eta} & \frac{\partial y}{\partial \eta} \end{bmatrix}$ is the Jacobian matrix, as derived in [27], [33], [34].

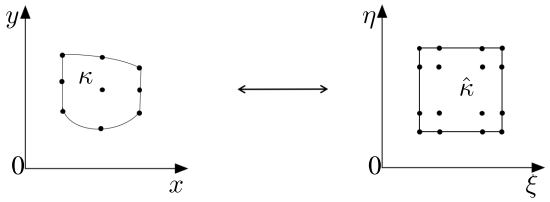

FIGURE 2. The 3rd-order curvilinear mapping between κ and $\hat{\kappa}$. (Left) A second-order geometrical curved element κ in the physical domain. (Right) The corresponding reference element $\hat{\kappa}$ for the 3-rd SEM ($N = 3$), where the 16 points are GLL points.

B. DISCRETE FORMS

In general, three unknown components u_j of the displacement field can be approximated by

$$u_j = \sum_{q=1}^{\mathrm{n}_{sj}} u_{j,q} \varphi_q^{(N)}(x, y) \tag{30}$$

where n_{sj} represents the number of nodal degrees of freedom (DOFs) of the component u_j for the solid region. Thus, the total number of DOFs in the solid region is $N_s = \sum_{j=1}^{3} N_{sj}$. Inserting (30) into (18), we arrive at the quadratic eigenvalue problems

$$[\gamma_z^2 \bar{\bar{A}}^s - \gamma_z \bar{\bar{B}}^s + (\bar{\bar{K}}^s + \bar{\bar{M}}^s) + \bar{\bar{T}}^s]\mathbf{u} = 0 \tag{31}$$

where $\boldsymbol{u} \triangleq [\boldsymbol{u}_1, \boldsymbol{u}_2, \boldsymbol{u}_3]^T$, $\mathbf{u}_j \triangleq (u_{j,1}, \cdots, u_{j,\mathrm{n}_{sj}})$, the subscript "$s$" means the solid region and $\bar{\bar{T}}$ is the boundary integral matrix, which is equal to zero when using the hard, the soft and the Bloch periodic boundary condition, and nonzero for the absorbing boundary condition. After the invertible mapping, the elemental matrices consist of the following parts

$$\begin{aligned}
(\bar{\bar{A}}_{ik}^{(\hat{\kappa})})_{pq} &= \int_{-1}^{1}\int_{-1}^{1} |\boldsymbol{J}| \hat{\varphi}_p^{\dagger} \ell_{3ik3} \hat{\varphi}_q \, d\xi d\eta \\
(\bar{\bar{B}}_{ik}^{(\hat{\kappa})})_{pq} &= \int_{-1}^{1}\int_{-1}^{1} |\boldsymbol{J}| \hat{\varphi}_p^{\dagger} (\ell_{3ik\alpha} \mathcal{J}_\alpha \hat{\varphi}_q) \, d\xi d\eta \\
&\quad - |\boldsymbol{J}| (\mathcal{J}_\alpha \hat{\varphi}_p)^{\dagger} (\ell_{\alpha ik3} \hat{\varphi}_q) d\xi d\eta \\
(\bar{\bar{K}}_{ik}^{(\hat{\kappa})})_{pq} &= -\int_{-1}^{1}\int_{-1}^{1} |\boldsymbol{J}| (\mathcal{J}_\alpha \hat{\varphi}_p)^{\dagger} (\ell_{\alpha ik\beta} \mathcal{J}_\beta \hat{\varphi}_q) d\xi d\eta \\
(\bar{\bar{M}}_{ik}^{(\hat{\kappa})})_{pq} &= \omega^2 \int_{-1}^{1}\int_{-1}^{1} |\boldsymbol{J}| \rho_{ik} \hat{\varphi}_p^{\dagger} \hat{\varphi}_q d\xi d\eta \\
(\bar{\bar{T}}_{ik}^{(\hat{\kappa})})_{pq} &= \mathrm{j}\omega \int_{-1}^{1} |\boldsymbol{J}_b| \hat{\varphi}_p^{\dagger} [\rho_{ik} C_T \\
&\quad + (C_L - C_T) \mathrm{n}_k \rho_{i\alpha} \mathrm{n}_\alpha] \hat{\varphi}_q d\xi
\end{aligned} \tag{32}$$

where $p, q = 1, 2 \cdots, N+1$, the superscript "$(\hat{\kappa})$" means the reference element and $\boldsymbol{J}_b$ arises from the mapping from any edges to reference domain $[-1, 1]$. Meanwhile, $\bar{\bar{T}}^s$ arising from the absorbing boundary condition is expressed in (32). Similarly, u_j, χ are written as

$$u_j^{(s)} = \sum_{q=1}^{\mathrm{n}_{sj}} u_{j,q}^{(s)} \varphi_q^{(s)}, \quad w^{(f)} = \sum_{q=1}^{\mathrm{n}_f} w_q^{(f)} \varphi_q^{(f)} \tag{33}$$

where n_f denotes the number of the total nodal DOFs for the fluid region. Substituting (33) into (28), we arrive at the fluid-solid coupling eigenvalue problem (34), as shown at the bottom of the next page, based on the Bloch periodic boundary condition, where $\bar{\bar{R}}^{(s,f)} = [\bar{\bar{R}}_1^{(s,f)}, \bar{\bar{R}}_2^{(s,f)}, \bar{\bar{R}}_3^{(s,f)}]^T$, $\bar{\bar{Q}}^{(f,s)} = [\bar{\bar{Q}}_1^{(f,s)}, \bar{\bar{Q}}_2^{(f,s)}, \bar{\bar{Q}}_3^{(f,s)}]$, $\boldsymbol{w} \triangleq (w_1, \cdots, w_{\mathrm{n}_f})$. The elemental matrices are given as following

$$(A_0^{(f)})_{pq} = \int_{-1}^{1}\int_{-1}^{1} |\boldsymbol{J}| \hat{\varphi}_p^{(f)\dagger} \rho_f^{-1} \hat{\varphi}_q^{(f)} d\xi d\eta$$

$$\begin{cases} \gamma_z^2 a_{ij}(u_j, \varphi) - \gamma_z [b_{ij}(u_j, \varphi) + I_1] + q_{ij}(u_j, \varphi) + I_2 + I_5^{fs} = 0 \\ \gamma_z^2 e(\chi, \psi) - f(\chi, \psi) + I_4 + I_4^{fs} = 0 \end{cases} \tag{28}$$

$$
\begin{aligned}
(K_0^{(f)})_{pq} &= -\int_{-1}^{1}\int_{-1}^{1} |\boldsymbol{J}|(\mathcal{J}_\alpha \hat{\varphi}_p^{(f)})^\dagger \rho_f^{-1}(\mathcal{J}_\alpha \hat{\varphi}_q^{(f)}) d\xi d\eta \\
(M_0^{(f)})_{pq} &= \int_{-1}^{1}\int_{-1}^{1} |\boldsymbol{J}|\hat{\varphi}_p^{(f)\dagger}\kappa^{-1}\omega^2\hat{\varphi}_q^{(f)} d\xi d\eta \\
(\bar{\bar{Q}}_i^{(f,s)})_{pq} &= \mathrm{j}\omega\int_{-1}^{1} |\boldsymbol{J}_b|\hat{\varphi}_p^{(f)\dagger}\mathrm{n}_i\hat{\varphi}_q^{(s)} d\xi \\
(\bar{\bar{R}}_i^{(s,f)})_{pq} &= \mathrm{j}\omega\int_{-1}^{1} |\boldsymbol{J}_b|\hat{\varphi}_p^{(s)\dagger}\hat{\varphi}_q^{(f)}\mathrm{n}_i d\xi
\end{aligned} \tag{35}
$$

The remaining elemental matrices can be obtained by replacing the superscript $(\hat{\kappa})$ of (32) with (s). After these matrices are assembled, the quadratic eigenvalue problems (34) is converted to a first order generalized eigenvalue problem (36), as shown at the bottom of the page, for γ_z referring to [38], where $\mathbf{I}$ and $\mathbf{0}$ denote the identity matrix and zero matrix. Then (36) can be solved by using the eigenvalue solver "eigs" in MATLAB based on ARPACK library routines.

IV. NUMERICAL RESULTS

In this section, several examples are presented to verify the high accuracy and efficiency of the SEM for simulating elastic waveguide problems. The memory, the number of DOFs and the accuracy of the SEM are compared with the commercial FEM solver COMSOL. Finally, we conduct a numerical experiment on an elastic matematerial(EMM) core which cannot be solved by COMSOL, because of the presence of anisotropic density. Before the experiments, there are some preparations. First, in the simulation of the Bloch periodic boundary condition waveguide problem, the wave vector is defined by

$$\mathbf{k} = k(\hat{x}\sin\theta\cos\phi + \hat{y}\sin\theta\sin\phi + \hat{z}\cos\theta)$$

where $k = \omega/v_i$, v_i is the velocity of the P wave or S wave in the background medium and (θ, ϕ) are the elevation and azimuthal angles of the propagation direction. Second, for convenience, we introduce the notations in our tables and figures:

1) v_p and v_s are the velocities of the P (longitudinal) wave and the S (transversal) waves.
2) ρ is the mass density.
3) λ and μ are Lamè constants.
4) $\mathrm{k}_{i,z}^N$ is the i-th eigenmode wavenumber k_z obtained in the z direction by the N-th order SEM.
5) The reference value $\bar{\mathrm{k}}_{i,z}^{10}$ is the solution of the 10th-order SEM with an extremely fine mesh.
6) The relative error is calculated by $|\mathrm{k}_{i,z}^N - \bar{\mathrm{k}}_{i,z}^{10}|/|\bar{\mathrm{k}}_{i,z}^{10}|$.

For the quadratic eigenvalue problems, the solver will provide two opposite eignvalues (γ_z and $-\gamma_z$). To determine the correct sign of the propagation constant, we introduce two quantities: the time averaged Poynting vector [39] $\mathbf{p} = \mathrm{Re}(-\mathrm{j}\omega\mathbf{u}\cdot\boldsymbol{\tau}^*)/2$ and the corresponding power $P_z = \int_\Gamma \hat{\mathbf{z}}\cdot\mathbf{p}dxdy$ in the cross section. The positive P_z is the criterion for choosing the correct sign of γ_z in the following numerical examples. The SEM is implemented by using Matlab on a MacBook Pro 2018 PC with 16 GB Memory and Intel Core i7 CPU. COMSOL was used for comparison on the same PC. The computational time and memory are displayed with the "tic", "toc" function and "memory" function in Matlab, respectively.

A. BLOCH PERIODIC UNIT CELL

In order to verify the accuracy and convergence of the proposed SEM, we first consider a simple inhomogeneous anisotropic waveguide with the Bloch periodic boundary condition. The Bloch periodic unit cell has many applications in lithography and the design of elastic metasurfaces, which act as a plate-like waveguide connecting two elastic half-spaces [40]. The configuration of the unit cell is shown in FIG. 3, where nine circular lead cores are embedded in the zinc square lattice. These circles with different radii are spaced one millimeter apart. The material properties are $\lambda_{\mathrm{Pb}} = 3.142 \times 10^{10}$ N/m^2, $\mu_{\mathrm{Pb}} = 5.986 \times 10^9$ N/m^2, $\rho_{\mathrm{Pb}} = 11340$ kg/m^3. The cladding is a transversely isotropic material with $\mathrm{C}_{11} = 16.5$ GPa, $\mathrm{C}_{12} = 3.1$ GPa, $\mathrm{C}_{13} = 5.0$ GPa, $\mathrm{C}_{33} = 6.2$ GPa, $\mathrm{C}_{55} = 3.96$ GPa and $\rho_{\mathrm{Zn}} = 2700$kg/m^3. The frequency $f = 5$ MHz and the unit cell is 2 cm containing multiple wavelengths, so that it is a relatively large scale problem.

The numerical results of $\mathrm{k}_{i,z}^N$ obtained by the 5th-order SEM, the 5th-order FEM in COMSOL and the 10th-order SEM are shown in Table 1 (the negligible imaginary part is not shown). In view of the maximum interpolation order of COMSOL is only 5, 10th-order SEM is taken as the reference value. It is observed that the 5th-order SEM matches excellently with both the 5th-order COMSOL and 10th-order SEM. On the other hand, as illustrated in Table 2, to achieve the similar accuracy, when searching for 20 modes at $f = 5$ MHz, COMSOL requires 1.5 times DOFs, 1.8 times CPU

$$
\{\gamma_z^2\begin{bmatrix}\bar{\bar{A}}^s & 0\\ 0 & A_0^f\end{bmatrix} - \gamma_z\begin{bmatrix}\bar{\bar{B}}^s & 0\\ 0 & 0\end{bmatrix} + \begin{bmatrix}\bar{\bar{K}}^s + \bar{\bar{M}}^s & \bar{\bar{R}}^{(s,f)}\\ \bar{\bar{Q}}^{(f,s)} & K_0^f + M_0^f\end{bmatrix}\}\begin{pmatrix}\boldsymbol{u}\\ \boldsymbol{w}\end{pmatrix} = 0 \tag{34}
$$

$$
\begin{bmatrix}\bar{\bar{B}}^s & \mathbf{0} & -\bar{\bar{K}}^s - \bar{\bar{M}}^s & -\bar{\bar{R}}^{(s,f)}\\ \mathbf{0} & \mathbf{0} & -\bar{\bar{Q}}^{(f,s)} & -K_0^f - M_0^f\\ \mathbf{I} & \mathbf{0} & \mathbf{0} & \mathbf{0}\\ \mathbf{0} & \mathbf{I} & \mathbf{0} & \mathbf{0}\end{bmatrix}\begin{bmatrix}\gamma_z\boldsymbol{u}\\ \gamma_z\boldsymbol{w}\\ \boldsymbol{u}\\ \boldsymbol{w}\end{bmatrix} = \gamma_z\begin{bmatrix}\bar{\bar{A}}^s & \mathbf{0} & \mathbf{0} & \mathbf{0}\\ \mathbf{0} & A_0^f & \mathbf{0} & \mathbf{0}\\ \mathbf{0} & \mathbf{0} & \mathbf{I} & \mathbf{0}\\ \mathbf{0} & \mathbf{0} & \mathbf{0} & \mathbf{I}\end{bmatrix}\begin{bmatrix}\gamma_z\boldsymbol{u}\\ \gamma_z\boldsymbol{w}\\ \boldsymbol{u}\\ \boldsymbol{w}\end{bmatrix} \tag{36}
$$

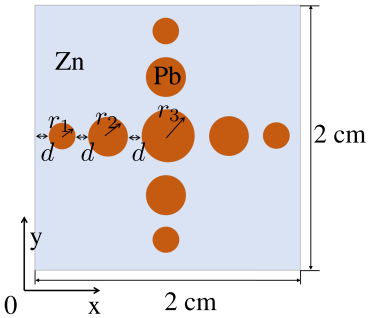

FIGURE 3. Schematic view of a unit cell with nine lead circles ($r_1 = 1$ mm, $r_2 = 1.5$ mm, $r_3 = 2$ mm). They are separated by the interval of $d = 1$ mm and are embedded in the anisotropic zinc. The square outer boundaries are set as the Bloch periodic condition.

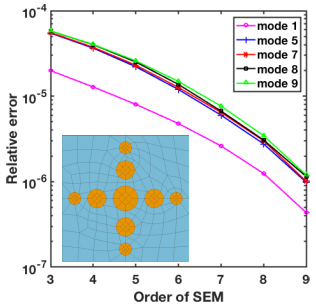

FIGURE 5. The second order curvilinear quadrilateral mesh with 244 elements and relative errors of eigenmodes obtained by using the different order SEM for the Bloch periodic boundary condition waveguide shown in FIG. 3.

TABLE 1. k_z (rad/s) of the elastic BPBC waveguide in FIG. 3 obtained by the SEM and COMSOL.

i	SEM-$k^5_{i,z}$	COMSOL-$k^5_{i,z}$	SEM-$\bar{k}^{10}_{i,z}$
1-2	4.3225E+04	4.3225E+04	4.3225E+04
3-10	4.3213E+04	4.3213E+04	4.3214E+04
11	4.3202E+04	4.3201E+04	4.3203E+04
12-13	4.3201E+04	4.3200E+04	4.3201E+04
14	4.3199E+04	4.3199E+04	4.3199E+04
15-22	4.3180E+04	4.3181E+04	4.3183E+04
DOF	18543	37458	73200

time and 1.3 times memory used by the SEM. Moreover, the comparison when twice the frequency $f = 10$ MHz is also shown in Table 2. We can also see that when the numbers of element and DOFs are taken to be similar, COMSOL is not as accurate as the SEM and requires a little more computational costs. Thus, the proposed SEM is more efficient than the FEM, mainly because of the spectral accuracy (the exponential convergence) of the SEM shown in FIG. 5. The magnitude distributions of $\mathbf{u}(x, y)$ for the 1st, 7th, 18th mode are displayed in FIG. 4. All of them propagate in the lead core with different radii.

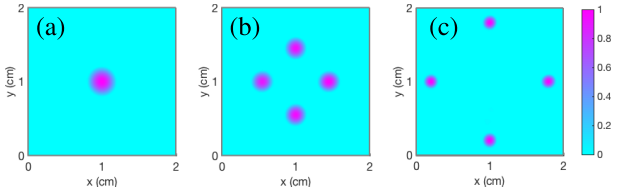

FIGURE 4. Magnitude distributions of $\mathbf{u}(x, y)$ corresponding to $k_{i,z}$ ($i = 1, 7, 18$) of the Bloch periodic boundary condition waveguide shown in FIG. 3. (a)-(c) correspond to the 1st, 7th and 18th mode.

B. RESONANT STRUCTURE OF AN EMM

In order to verify that our SEM solver is accurate and efficient for the inhomogeneous waveguide with solid-fluid coupling and Bloch periodic boundary condition, we first consider a resonant structure in the building block of a left-handed material proposed in [21]. This kind of resonant structure will bring negative elastic parameters within a certain frequency range and the cross section of the unit cell, a rubber coated water cylinder embedded in a foam host, is shown in FIG. 6. The lattice constant is a and the radius of the rubber and water is $0.32a$ and $0.24a$, respectively. When we set $a = 1$ m, the corresponding frequency is chosen as 34.887 Hz referring to [21]. In addition, the material parameters are listed in Table 3 and the Bloch periodic boundary condition is used in the example, $(\theta, \phi) = (0, 0)$ and $k = \omega/v_s$, v_s is the velocity of S wave in the foam. Table 4 shows that the numerical solutions of this inhomogeneous isotropic waveguide with Bloch periodic boundary condition obtained by the SEM and COMSOL agrees well. On the other hand, as illustrated in Table 5, the proposed SEM is more efficient than the FEM in terms of the DOFs and memory. Moreover, from the subgraph (a) and (c) of FIG. 7, we can see that there is a quadrupolar resonance in the rubber region for the first mode produced by the P wave, due to the much smaller v_p of the rubber than those in the background foam and the water core. Besides, as shown in the subgraph (b) and (d) of FIG. 7, a total reflection occurs at the boundary between the rubber region and the water core for the second mode, because of the much larger v_p of the water in Table 3.

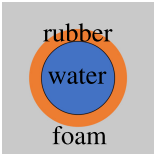

FIGURE 6. The cross section of the resonant structure for a left-hand material with a rubber coated water cylinder embedded in a foam host, with their material properties listed in Table 3.

C. OPTICAL FIBER MODEL

Next, to verify the absorbing boundary condition formulation for an open (unbounded) inhomogeneous isotropic waveguide, we consider the optical fiber. It is a common optical waveguide consisting of the cladding and the fiber core, and its elastic waveguide properties are of significant interest [41], [42]. The cross section of the optical fiber is shown in FIG. 8, which consists of the core and the cladding. The radius of the core and the cladding is $a = 4.1$ μm and

TABLE 2. The comparison of the FEM and the SEM for the elastic Bloch periodic boundary condition waveguide in FIG. 3.

	Frequency (MHZ)	# of Elements	DOFs	Relative Error	Time (s)	Memory (GB)
FEM(N=5)	5	243	17448	1.2E-5	44	1.92
FEM(N=5)	5	350	26793	9.5E-6	72	2.1
SEM(N=5)	5	244	18300	8.0E-6	40	1.6
FEM(N=5)	10	1307	98538	7.0E-7	276	3.27
SEM(N=8)	10	244	46848	4.8E-7	160	2.9

TABLE 3. Parameters for the resonant structures in FIG. 6.

	λ (N/m^2)	μ (N/m^2)	ρ (kg/m^3)	v_p (m/s)	v_s (m/s)
foam	6×10^6	3×10^6	115	323	161.5
rubber	6×10^5	4×10^4	1300	22.8	5.5
water	2.25×10^9	0	1000	1500	0

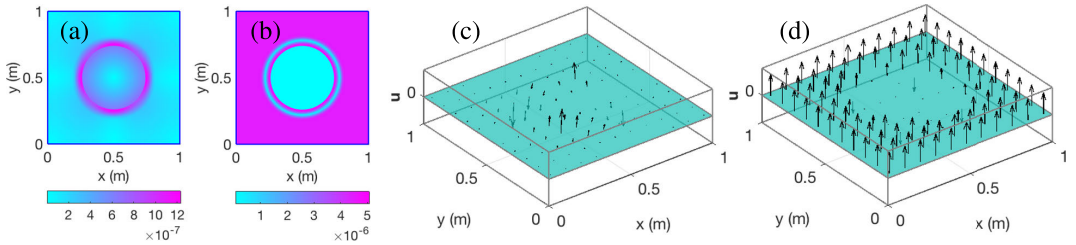

FIGURE 7. The distributions of u correspond to the first two modes in the elastic resonant structure waveguide in FIG. 6. The first mode in (a) and (c) exhibits a quadrupolar resonance in the rubber region. The second mode in (b) and (d) shows a total reflection at the interface between the rubber region and the water region.

TABLE 4. The first two values of k_z (rad/s) of the elastic resonant structure waveguide in FIG. 6 obtained by the SEM and COMSOL.

i	SEM - $k^5_{i,z}$	COMSOL - $k^5_{i,z}$	SEM - $\bar{k}^{10}_{i,z}$
1	2.85094	2.85087	2.85093
2	0.73831	0.73831	0.73831
DOF	18523	20401	444278

$3a = 12.3\ \mu$m, respectively; the cladding is pure SiO_2 and the core is filled with one of the three different materials as shown in Table 6. The SEM is employed to simulate the elastic waveguide properties of this optical fiber. Besides, to verify the accuracy and effectiveness of the SEM for solving the solid-fluid system, a fluid cladding is also considered. The material parameters are included in Table 6. In order to simulate the unbounded waveguide structure, the absorbing boundary condition is used to truncate the cladding so that the simulated structure mimics an infinite cladding region.

1) NORMAL ELASTIC MATERIALS

First, to verify the accuracy of the SEM solver for the inhomogeneous open waveguide problems, we conduct a numerical experiment on the actual optical quartz fiber model consisting of cladding 1 and core 1, and the frequency is chosen as 3 GHz as in realistic application [43]. The agreement among the three results in Table 7 verifies the accuracy of our scheme. Besides, we observe that the real part of the higher-order

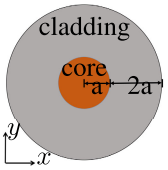

FIGURE 8. The cross section of the optical fiber (a = 4.1 μm), with an unbounded cladding truncated by an absorbing boundary condition at $r = 3a$. The core and cladding materials can take the combination of materials listed in Table 6.

mode gradually decreases while the imaginary part falling into different orders of magnitude gradually increases. The phenomenon indicates that the energy loss of the higher-order mode gradually increases. The relative errors and computational costs of the SEM and the FEM are illustrated in Table 8. For a similar mesh, the proposed 3rd-order SEM and 4th-order FEM can achieve similar accuracy (3E-6). The corresponding memory used by FEM is more than SEM, illustrating the proposed SEM is more efficient than FEM. Moreover, it can be observed that the 6th-order SEM can achieve higher accuracy (3E-7) with less memory, due to the spectral accuracy of the SEM solver. Moreover, waves are well absorbed at the outer absorbing boundary.

2) DOUBLE NEGATIVE INDEX ELASTIC METAMATRIAL (EMM) CORE

Second, for the same size model, we now consider the effects of the EMM core with a negative index. We design

TABLE 5. The comparison of FEM and SEM for the elastic resonant structure waveguide in FIG. 6.

	# of Elements	DOFs	Relative Error	Memory (GB)
FEM(N=5)	308	20401	1.8E-5	1.33
FEM(N=5)	408	25601	8.0E-6	1.35
SEM(N=5)	297	18523	5.6E-6	0.88

TABLE 6. Parameters for the cores and claddings of the optical fiber in FIG. 8.

	v_p (m/s)	v_s (m/s)	ρ (kg/m^3)	λ (N/m^2)	μ (N/m^2)
core 1 (impure SiO_2)	5794.626	3644.85	2291.25	1.6057×10^{10}	30.44×10^9
core 2 (EMM)	829.89	532.53j	-1481	-1.86×10^9	0.42×10^9
core 3 (normal)	1202	532.53	1481	1.30×10^9	0.42×10^9
cladding 1 (SiO_2)	5970	3760	2201	1.6212×10^{10}	31.13×10^9
cladding 2 (water)	1500	0	1000	2.25×10^9	0

TABLE 7. k_z (Mrad/s) of the elastic fiber-optics waveguide in FIG. 8 obtained by the SEM and COMSOL for core 1 and cladding 1 listed in Table 6.

i	SEM -$k_{i,z}^5$	COMSOL - $k_{i,z}^5$	SEM - $\bar{k}_{i,z}^{10}$
1-2	5.1478-3.8741E-11j	5.1478-3.8627E-11j	5.14780-3.8606E-11j
3	5.1127-7.1091E-10j	5.1127-7.1090E-10j	5.1127-7.1090E-10j
4-5	5.1119-9.6837E-10j	5.1119-9.6650E-10j	5.1119-9.6616E-10j
6	5.1116-1.2307E-09j	5.1116-1.2265E-09j	5.1116-1.2256E-09j
7-8	5.0670-3.7985E-08j	5.0670-3.7920E-08j	5.0670-3.7907E-08j
DOF	33648	33447	249303

TABLE 8. The comparison of FEM and SEM for the elastic fiber-optics waveguide in FIG. 8 with core 1 and cladding 1 listed in Table 6.

	# of Elements	DOFs	Relative Error	Memory (GB)
FEM(N=3)	112	3207	3.8E-5	1.37
FEM(N=4)	112	5619	1.9E-6	1.42
SEM(N=3)	107	2982	3.7E-6	0.79
SEM(N=6)	107	11739	3.0E-7	1.04

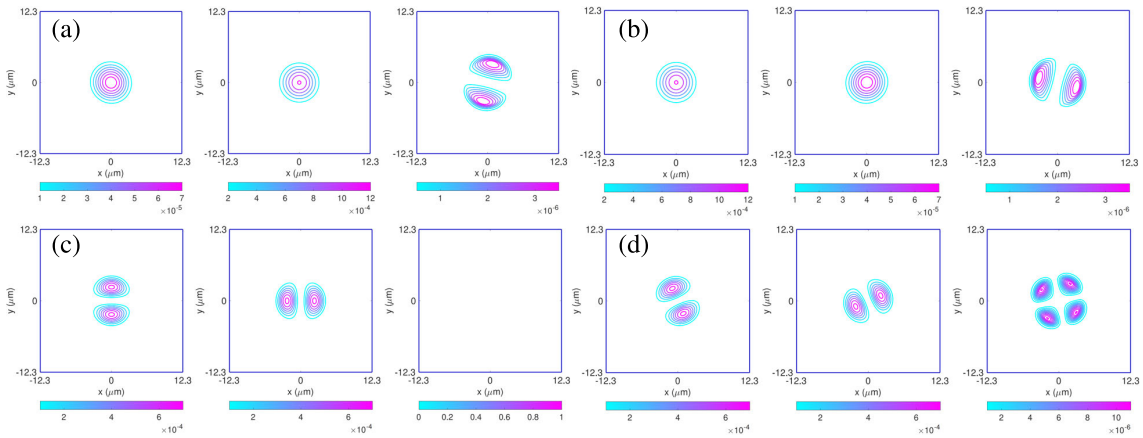

FIGURE 9. Contour maps of u_x, u_y, u_z in the open fiber-optics waveguide problem in FIG. 8 with an impure SiO_2 core 1. (a)-(d) correspond to the first to the fourth mode. No impurity shown in the contour maps indicate that no spurious modes exist and waves are well absorbed at the outer absorbing boundary.

an example on a simultaneously negative mass density and bulk modulus EMM core 2 constructed by reference [18], embedded in Cladding 1 in Table 6. The frequency is chosen as 0.3 GHz. Through calculating the velocities of P-wave and S-wave respectively shown in Table 6, we find the velocity of S-wave is an imaginary number, thus the S-wave is forbidden in this material. Again, $k_{i,z}^N$ ($N = 5,10$) obtained by the two methods are shown in Table 9. It is observed that the SEM solution matches excellently with the reference results and the COMSOL's results, verifying that our scheme is suitable

TABLE 9. k_z (Mrad/s) of the elastic waveguide with either EMM core 2 or core 3 and cladding 1 in FIG. 8 obtained by the SEM and COMSOL.

	EMM core 2			core 3	
i	SEM-$k^5_{i,z}$	COMSOL-$k^5_{i,z}$	SEM-$\bar{k}^{10}_{i,z}$	SEM-$k^5_{i,z}$	COMSOL-$k^5_{i,z}$
1	-3.0272216	-3.0272236	-3.0272209	3.4871638	3.4871639
2	-3.0139166	-3.0139190	-3.0139156	3.4142176	3.4142180
3	-2.9737232	-2.9737341	-2.9737218	3.4041896	3.4041900
4	-2.9056978	-2.9057024	-2.9056937	3.3968465	3.3968469
5	-2.8080154	-2.8080351	-2.8080125	3.3021688	3.3021695
DOF	11433	24138	189963	11433	24138

TABLE 10. The comparison of FEM and SEM with EMM core 2 in Table 9.

	# of Elements	DOFs	Relative Error	Memory (GB)
FEM(N=5)	157	12018	5.64E-6	1.39
FEM(N=5)	317	24138	8.93E-7	1.62
SEM(N=5)	150	11433	8.16E-7	1.19

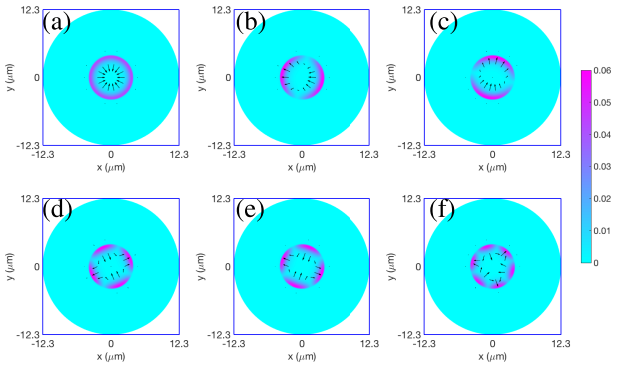

FIGURE 10. Magnitude distributions of $\mathbf{u}(x, y)$ for eignmodes corresponding to $k_{i,z}$ ($i = 1, \cdots, 6$) obtained in the open fiber-optics waveguide problem with EMM core 2 in cladding 1 in FIG. 8. (a)-(f) correspond to the first to the sixth mode. All of them propagate only at the interface between the core and cladding because of the presence of the negative index material, different from the normal material core 3 in FIG. 11.

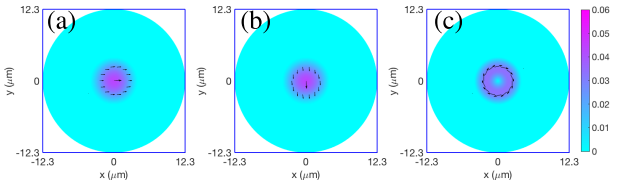

FIGURE 11. Magnitude distributions of $\mathbf{u}(x, y)$ for eignmodes corresponding to $k_{i,z}$ ($i = 1, 2, 3$) obtained in the open fiber-optics waveguide problem in FIG. 8 with the normal material core 3 in cladding 1. (a)-(c) correspond to the first to the third mode. In the contrast to the EMM core 2 in FIG. 10, the fundamental mode found in the normal material open fiber-optics waveguide is concentrated in the whole core region.

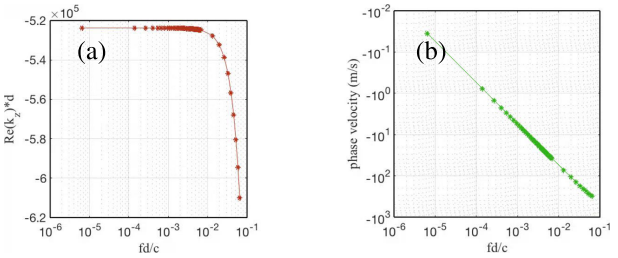

FIGURE 12. The dispersion curves versus with frequency ($d = 2a$, $c = v_s$ of cladding 1) for the fundamental mode in the waveguide with EMM core 2 and cladding 1 in FIG. 8. (a) The real part of k_z. Within the low frequency $fd/c \in [6.5 \times 10^{-6}, 9 \times 10^{-3}]$, the real part of k_z does not vary with the frequency. (b) The phase velocity. The negative value means the direction of the phase velocity is $-\hat{z}$, antiparallel to the $+\hat{z}$. Thus, the backward wave propagation phenomenon is found in this mode.

for the negative index materials. Meanwhile, as illustrated in Table 10, DOFs and the memory used by COMSOL with 5th-order basis functions is 2.1 and 1.4 times more than 5th-order SEM to achieve the similar accuracy (8E-7). Evidently, it shows the high computation efficiency of the SEM. Furthermore, the magnitude distributions of $\mathbf{u}(x, y)$ corresponding to $k_{i,z}$ ($i = 1, \cdots, 6$) with EMM core 2 are plotted in FIG. 10. On the other hand, instead of core 2, we conduct another experiment on core 3, whose density and bulk modulus are positive. The agreement in Table 10 verifies the accuracy of the results. FIG. 11 plots the distribution of $\mathbf{u}$ corresponding to $k_{i,z}$ ($i = 1, 2, 3$) with core 3. In contrast to the previous configuration, we observe in FIG. 10 that these modes in the waveguide of EMM core 2 propagate only at the interface between the core and cladding because of the presence of the negative index material.

Furthermore, we notice that one propagation mode exists under low frequencies ($fd/c \in [6.5 \times 10^{-6}, 9 \times 10^{-3}]$, $d = 2a$) as shown in FIG. 12. Within this frequency range, different from normal elastic materials, the increase of the frequency does not alter the distribution interval of the real part of k_z (the phase constant $\beta_z = -5.23 \times 10^5$) with the negligible imaginary part (the attenuation constant α_z) on the basis of the positive P_z. Through the observation in FIG. 13, we can find the propagation mode is caused by the P wave and concentrated in the core. In addition, in order to explain the existence of this mode, the phase velocity $v_p = \omega/\beta_z$ is shown in FIG. 12 (b). It can be found that this mode exhibits

TABLE 11. $k_z(\times 10^5)$ for core 3 in water cladding in FIG. 8 obtained by the SEM and FEM.

i	SEM-$k^5_{i,z}$	COMSOL-$k^5_{i,z}$	SEM-$\bar{k}^{10}_{i,z}$
1	8.442953-1.01951E-06j	8.442940-1.86170E-05j	8.442953-1.01950E-06j
2	7.189511-8.99567E-06j	7.189528-1.14219E-04j	7.189514-8.99557E-06j
3	7.079197	7.079197	7.079197
4	7.047610-4.23577E-05j	7.048429-9.52793E-04j	7.047614-4.23571E-05j
Fluid-DOF	5630	50730	88420
Solid-DOF	6618	30073	53463

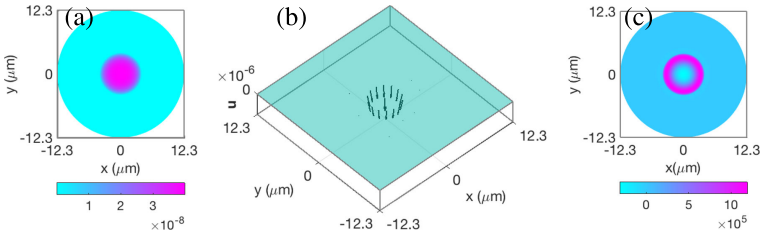

FIGURE 13. The distributions for $\mathbf{u}(x, y)$ for the first eigenmode at low frequency when the waveguide is filled with EMM core 2 in Figure 12. This mode remains the same in the frequency range of $fd/c \in [6.5 \times 10^{-6}, 9 \times 10^{-3}]$. (a) The magnitude distribution of $\mathbf{u}(x, y)$. (b) The 3D vector of u. (c) The z-component of Poynting vector.

backward wave propagation in the cross section, which is defined as the phase velocity direction $(-\hat{z})$ antiparallel to the Poynting vector $(+\hat{z})$, caused by the negative-index materials [44]. Hence, different from normal elastic materials, the application of EMMs will bring some special eigenmodes in the elastic waveguide.

3) SOLID-FLUID COUPLING MODEL

In the previous case, the cladding was assumed unbounded, which may not be realistic. Actually, the external medium of the most practical open waveguide problems is fluid (for example, either air or water). Therefore, here we examine the same size model to verify the fluid-solid coupling system of the open waveguide problems at the frequency of 60 MHz. In this case, the cross section consists of the solid core 3 and the fluid cladding 2. Noting that COMSOL does not provide the absorbing boundary condition in the mode analysis of the acoustic module. So for comparison, we set the impedance value of the plane wave as an approximation in COMSOL when the outer boundary is far enough. The agreement is good as illustrated in Table 11, demonstrating that the proposed SEM is capable of treating the absorbing boundary condition solid-fluid problem. Besides, the relative errors $(|k^N_{i,z} - \bar{k}^{10}_{i,z}|/|\bar{k}^{10}_{i,z}|)$ obtained by different orders of SEM confirm the exponential convergence in FIG. 14. Next, we give a detail discussion about the third mode, whose attenuation constant is almost zero. First, as observed in FIG. 15, different from other modes, the propagation of this mode concentrates in the core. The reason for this phenomenon is that the third mode may be caused by the transversal wave, which cannot be transmitted into the fluid region. Moreover, as indicated in [33], for an exact integration [$(N+1)$th-order GLL quadrature in each element] of the second-order

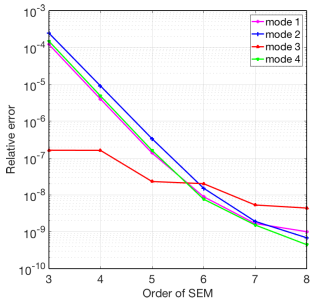

FIGURE 14. Relative errors of the first four modes of the solid-fluid open fiber-optics waveguide problem in FIG. 8. Note that the error curve of the third mode are straight lines if one groups the even and odd orders separately, because the even and odd orders have different offsets.

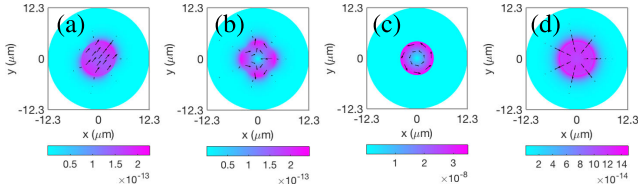

FIGURE 15. Magnitude distributions of $\mathbf{u}(x, y)$ for these eignmodes obtained in solid (core 3) - fluid (Water) open fiber-optics waveguide problem in FIG. 8. (a)-(d) correspond to the first to the fourth modes. Note that different from other modes, the propagation of the third mode concentrates in the core.

geometrical modeling, the errors of mode 3 are straight lines if one groups the even and odd orders separately, and the even and odd orders have different offsets. Therefore the relative error of this mode is reasonable.

D. EMM WITH ANISOTROPIC DENSITY

In addition to the metamaterials with negative index discussed above, the metamaterials with anisotropic mass density have

attracted more and more attention recently. Because the equivalent model with effective anisotropic mass density can describe the dynamic behavior of the original lattice system in all directions. Hence, we conduct one numerical experiment on one anisotropic density core that cannot be simulated by some traditional numerical methods. Besides, in this section, the formulation of phase velocity obtained by elastic tensor C and isotropic density ρ in literature [45] is extended to one suitable for anisotropic density $\bar{\bar{\rho}} = (\rho_{ij})_{3\times3}$. Note that the explanations of the symbols are referred to reference [45]. Starting with time domain governing equation

$$\bar{\bar{\rho}} \cdot \frac{\partial^2 \mathbf{u}}{\partial t^2} - \nabla \cdot \boldsymbol{\tau} = 0 \tag{37}$$

Multiplying both sides by the inverse of $\bar{\bar{\rho}}$, the scalar expressions for a homogeneous medium are arrived at

$$\frac{\partial^2 u_i}{\partial t^2} = (\bar{\bar{\rho}}^{-1})_{im} \cdot c_{mjkl} \frac{\partial^2 u_k}{\partial x_l \partial x_j} \tag{38}$$

After denoting $\Gamma_{ik} = c_{ijkl} n_j n_l$, where n_j is the component of the unit propagation vector $\mathbf{n}$ and multiplying both sides by p_l, the components of the unit polarization vector colinear with the displacement. The final eigenvalue formulation is obtained

$$[(\bar{\bar{\rho}}^{-1})_{im} \cdot \Gamma_{ml} p_l - v^2 \delta_{il}] p_l = 0 \tag{39}$$

where v^2 is the eigenvalue.

The cross section centered at (0,0) m is shown in FIG. 16; the width of the square cladding and the square core is 0.5 m and 0.11 m, respectively. The cladding is zinc with isotropic material parameters $\{v_p, v_s\} = \{4820.7, 2361.6\}$ m/s and the mass density is 7100 kg/m^3. The core is an anisotropic EMM with the effective elastic coefficients $C_{11} = 36.63$ GPa, $C_{12} = 5.57$ GPa, $C_{13} = 13.53$ GPa, $C_{22} = 18.83$ GPa, $C_{23} = 7.84$ GPa, $C_{33} = 48.38$ GPa, $C_{44} = 12.41$ GPa, $C_{55} = 6.69$ GPa, $C_{66} = 2.272$ GPa. The frequency we choose is $f = 16$ kHz and corresponding effective anisotropic mass density represent $\rho_{\text{EMM}} = \text{diag}\{6277, 3168, 2700\}$ kg/m^3 according to [20]. The anisotropic mass density is frequency-dependent and caused by the different locally resonant frequencies along different directions in the microstructure design, depending on the inverse proportional function $\rho_{\text{eff},i} = a + b/(\omega_i^2 - \omega^2)$ [20], [46], where a, b are the positive constants given by the detailed model parameters and ω_i is the locally resonance frequency along the i direction ($i = x, y, z$). Note that ω_1 is the smallest, the ρ_{EMM} is certainly produced by the frequency below and close to the ω_1, leading to the resonance phenomena dominated by the u_x. Besides, the velocity of EMM along $\mathbf{n} = (0, 0, 1)$ calculated through equation (37) is $\{v_p, v_{s1}, v_{s2}\} = \{4233, 1979.2, 1032.4\}$ m/s, smaller than the cladding. Therefore, the absorbing boundary condition is used to truncate the cladding.

First, the good agreement between the 5th-order SEM numerical results and the 10th-order results of the extremely fine mesh is demonstrated in Table 12. Then, the relative errors of the first three modes plotted in FIG. 17 indicate

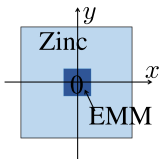

FIGURE 16. The cross section of the anisotropic density waveguide consist of a square EMM core and an unbounded Zinc cladding truncated by a square outer absorbing boundary condition boundary.

TABLE 12. $\mathrm{k}^{\mathrm{N}}_{i,z}$ of the anisotropic mass density EMM waveguide problem in FIG. 16.

i	SEM - $\mathrm{k}^{5}_{i,z}$	SEM - $\bar{\mathrm{k}}^{10}_{i,z}$
1	79.78808-6.2E-10j	79.78866-6.2E-10j
2	73.91172-1.1E-09j	73.91355-1.1E-09j
3	63.19895-1.3E-07j	63.20232-1.3E-07j
Mesh	289	625
DOF	22188	189003

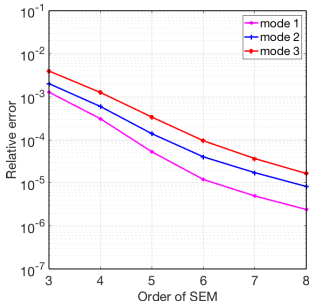

FIGURE 17. Relative errors of the first three modes for the anisotropic mass density EMM core waveguide problem in FIG. 16.

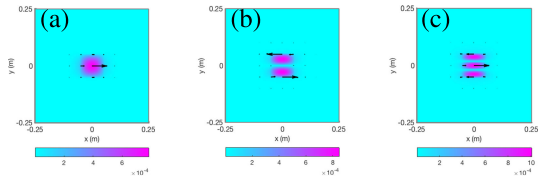

FIGURE 18. Magnitude distributions of $\mathbf{u}$ correspond to $\mathrm{k}_{i,z}$ ($i = 1, 2, 3$) of the anisotropic density EMM core in FIG. 16. (a)-(c) correspond to the first to the third modes. All of them are dominated by u_x. In contrast to a normal material core, no modes dominated by u_y and u_z are found in this EMM waveguide.

the exponential convergence. Moreover, the magnitude distributions of $\mathbf{u}$ are plotted in FIG. 18 and all of them in the xy plane are along the x direction and dominated by the x-component of the $\mathbf{u}$. On the other hand, we conduct another experiment on an normal anisotropic elastic core with the isotropic mass density $\rho = 3772.5$ kg/m^3 (the geometric average $\sqrt[3]{\prod_{i=1}^{3} \rho_{ii}}$) and the same elastic coefficients C. The magnitude distributions of $\mathbf{u}$ in this waveguide with normal materials are plotted in FIG. 19 and they are dominated by the components along three principal axis respectively. In contrast to the configuration with an EMM core, it can be found that the propagation mode dominated by u_y, u_z shown

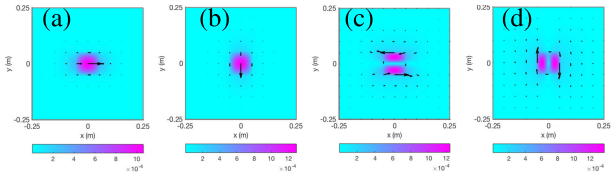

FIGURE 19. Magnitude distributions of **u** for eignmodes $k_{i,z}$ ($i = 1, \cdot, 4$) obtained in an open elastic waveguide problem with a normal isotropic density core with the EMM core in FIG. 16 replaced by an isotropic mass density $\rho = 3772.5$ kg/m^3. (a)-(d) correspond to the first to the fourth modes. Note that the 2nd, 4th modes dominated by u_y and u_z respectively are absent in the EMM waveguide in FIG. 18.

in FIG. 19 (c),(d) cannot be obtained in the example with the anisotropic mass density core. The phenomena are due to the difference between the EMM core and the normal core in view of the locally resonance frequencies in each principal axis, which is caused by the different mass density tensors. In conclusion, the above explains the phenomena caused by the use of the EMM core with the anisotropic mass density and demonstrates the rationality of our results.

V. CONCLUSION

This paper presents a spectral element method (SEM) solver for the general elastic matematerials (EMM) waveguide problems with negative index and anisotropic mass density as well as normal materials. The solver can treat inhomogeneous and anisotropic solids, but also include the fluid-solid coupling. Meanwhile, the discussions about four boundary conditions (the hard, the soft, the Bloch periodic, the absorbing boundary condition) are provided. Both excellent agreement between SEM results and those from the commercial FEM solver COMSOL and less computational costs are demonstrated in the numerical validations. Moreover, some interesting phenomena brought by the application of the EMM can be observed in the numerical experiments, for instance, unusual modes generated by the negative refractive or common modes eliminated by the anisotropic mass density.

REFERENCES

[1] C. Baron and S. Naili, "Propagation of elastic waves in a fluid-loaded anisotropic functionally graded waveguide: Application to ultrasound characterization," *J. Acoust. Soc. Amer.*, vol. 127, no. 3, pp. 1307–1317, Mar. 2010.
[2] Z. Su, L. Ye, and Y. Lu, "Guided Lamb waves for identification of damage in composite structures: A review," *J. Sound Vib.*, vol. 295, nos. 3–5, pp. 753–780, 2006.
[3] S. Banerjee, F. Ricci, E. Monaco, and A. Mal, "A wave propagation and vibration-based approach for damage identification in structural components," *J. Sound Vib.*, vol. 322, nos. 1–2, pp. 167–183, Apr. 2009.
[4] J. Miklowitz, *The Theory of Elastic Waves and Waveguides*. Amsterdam, The Netherlands: Elsevier, 2012.
[5] J. He, D. Homa, G. Pickrell, and A. Wang, "Coupled mode analysis for 3D stress-free elastic acoustic waveguide," *IEEE Access*, vol. 7, pp. 117796–117803, 2019.
[6] X. Xining, Z. Lu, X. Bo, Y. Zujun, and Z. Liqiang, "An ultrasonic guided wave mode excitation method in rails," *IEEE Access*, vol. 6, pp. 60414–60428, 2018.
[7] J. Liu, W. Jiang, N. Liu, and Q. H. Liu, "Mixed spectral-element method for the waveguide problem with Bloch periodic boundary conditions," *IEEE Trans. Electromagn. Compat.*, vol. 61, no. 5, pp. 1568–1577, Oct. 2019.
[8] F. Fesharaki, T. Djerafi, M. Chaker, and K. Wu, "Guided-wave properties of mode-selective transmission line," *IEEE Access*, vol. 6, pp. 5379–5392, 2018.
[9] R. Kirby, "Transmission loss predictions for dissipative silencers of arbitrary cross section in the presence of mean flow," *J. Acoust. Soc. Amer.*, vol. 114, no. 1, pp. 200–209, Jul. 2003.
[10] P. Lagasse, "Higher-order finite-element analysis of topographic guides supporting elastic surface waves," *J. Acoust. Soc. Amer.*, vol. 53, no. 4, pp. 1116–1122, 1973.
[11] A. S. Kosmodamianskii, I. A. Moiseenko, and R. R. Troyan, "Dispersion spectrum of an anisotropic waveguide with sector-shaped cross section and fixed boundary," *Int. Appl. Mech.*, vol. 41, no. 9, pp. 995–999, Sep. 2005.
[12] H. Gravenkamp, H. Man, C. Song, and J. Prager, "The computation of dispersion relations for three-dimensional elastic waveguides using the scaled boundary finite element method," *J. Sound Vib.*, vol. 332, no. 15, pp. 3756–3771, Jul. 2013.
[13] A.-C. Hladky-Hennion, P. Langlet, R. Bossut, and M. de Billy, "Finite element modelling of radiating waves in immersed wedges," *J. Sound Vib.*, vol. 212, no. 2, pp. 265–274, 1998.
[14] M. Mazzotti, A. Marzani, and I. Bartoli, "Dispersion analysis of leaky guided waves in fluid-loaded waveguides of generic shape," *Ultrasonics*, vol. 54, no. 1, pp. 408–418, Jan. 2014.
[15] A. V. Astaneh and M. N. Guddati, "Dispersion analysis of composite acousto-elastic waveguides," *Compos. B, Eng.*, vol. 130, pp. 200–216, Dec. 2017.
[16] H. Gravenkamp, C. Birk, and C. Song, "Computation of dispersion curves for embedded waveguides using a dashpot boundary condition," *J. Acoust. Soc. Amer.*, vol. 135, no. 3, pp. 1127–1138, 2014.
[17] Y. Liang, Y. Li, Y. Liu, Q. Han, and D. Liu, "Investigation of wave propagation in piezoelectric helical waveguides with the spectral finite element method," *Compos. B, Eng.*, vol. 160, pp. 205–216, Mar. 2019.
[18] X. N. Liu, G. K. Hu, G. L. Huang, and C. T. Sun, "An elastic metamaterial with simultaneously negative mass density and bulk modulus," *Appl. Phys. Lett.*, vol. 98, no. 25, Jun. 2011, Art. no. 251907.
[19] R. Zhu, Y. Y. Chen, Y. S. Wang, G. K. Hu, and G. L. Huang, "A single-phase elastic hyperbolic metamaterial with anisotropic mass density," *J. Acoust. Soc. Amer.*, vol. 139, no. 6, pp. 3303–3310, Jun. 2016.
[20] R. Zhu, X. N. Liu, G. L. Huang, H. H. Huang, and C. T. Sun, "Microstructural design and experimental validation of elastic metamaterial plates with anisotropic mass density," *Phys. Rev. B, Condens. Matter*, vol. 86, no. 14, Oct. 2012, Art. no. 144307.
[21] Y. Wu, Y. Lai, and Z.-Q. Zhang, "Elastic metamaterials with simultaneously negative effective shear modulus and mass density," *Phys. Rev. Lett.*, vol. 107, no. 10, Sep. 2011, Art. no. 105506.
[22] J.-H. Sun and T.-T. Wu, "Propagation of acoustic waves in phononic-crystal plates and waveguides using a finite-difference time-domain method," *Phys. Rev. B, Condens. Matter*, vol. 76, no. 10, Sep. 2007, Art. no. 104304.
[23] F. Moser, L. J. Jacobs, and J. Qu, "Modeling elastic wave propagation in waveguides with the finite element method," *NDT & E Int.*, vol. 32, no. 4, pp. 225–234, Jun. 1999.
[24] F. Treyssède, "Numerical investigation of elastic modes of propagation in helical waveguides," *J. Acoust. Soc. Amer.*, vol. 121, no. 6, pp. 3398–3408, 2007.
[25] I. Bartoli, A. Marzani, F. L. D. Scalea, and E. Viola, "Modeling wave propagation in damped waveguides of arbitrary cross-section," *J. Sound Vib.*, vol. 295, no. 3, pp. 685–707, 2006.
[26] W. Ostachowicz, P. Kudela, M. Krawczuk, and A. Zak, *Guided Waves in Structures for SHM: The Time-Domain Spectral Element Method*. Hoboken, NJ, USA: Wiley, 2012, pp. 47–92, doi: 10.1002/9781119965855.
[27] L. Shi, Y. Zhou, J.-M. Wang, M. Zhuang, N. Liu, and Q. H. Liu, "Spectral element method for elastic and acoustic waves in frequency domain," *J. Comput. Phys.*, vol. 327, pp. 19–38, Dec. 2016.
[28] D. Komatitsch, J. P. Vilotte, R. Vai, J. M. Castillo-Covarrubias, and F. J. Sánchez-Sesma, "The spectral element method for elastic wave equations—Application to 2-D and 3-D seismic problems," *Int. J. Numer. Methods Eng.*, vol. 45, no. 9, pp. 1139–1164, 1999.
[29] D. Komatitsch, C. Barnes, and J. Tromp, "Wave propagation near a fluid-solid interface: A spectral-element approach," *Geophysics*, vol. 65, no. 2, pp. 623–631, Mar. 2000.
[30] R. Hu and C. Oskay, "Spectral variational multiscale model for transient dynamics of phononic crystals and acoustic metamaterials," *Comput. Methods Appl. Mech. Eng.*, vol. 359, Feb. 2020, Art. no. 112761.

[31] G. Seriani and E. Priolo, "Spectral element method for acoustic wave simulation in heterogeneous media," *Finite Elements Anal. Des.*, vol. 16, nos. 3–4, pp. 337–348, Jun. 1994.
[32] G. Seriani and S. P. Oliveira, "DFT modal analysis of spectral element methods for acoustic wave propagation," *J. Comput. Acoust.*, vol. 16, no. 4, pp. 531–561, Dec. 2008.
[33] J. H. Lee and Q. H. Liu, "An efficient 3-D spectral-element method for Schrödinger equation in nanodevice simulation," *IEEE Trans. Comput.-Aided Design Integr. Circuits Syst.*, vol. 24, no. 12, pp. 1848–1858, Dec. 2005.
[34] J.-H. Lee, T. Xiao, and Q. H. Liu, "A 3-D spectral-element method using mixed-order curl conforming vector basis functions for electromagnetic fields," *IEEE Trans. Microw. Theory Techn.*, vol. 54, no. 1, pp. 437–444, Jan. 2006.
[35] M. Conry. *Notes on Wave Propagation in Anisotropic Elastic Solids*. Accessed: May 2021. [Online]. Available: https://www.acronymchile.com/elasticity.html
[36] J. Niu, Y. Ren, and Q.-H. Liu, "Spectral element boundary integral method with periodic layered medium dyadic Green's function for multiscale nano-optical scattering analysis," *Opt. Exp.*, vol. 25, no. 20, pp. 24199–24214, 2017.
[37] M. Luo, Q. H. Liu, and Z. Li, "Spectral element method for band structures of two-dimensional anisotropic photonic crystals," *Phys. Rev. E, Stat. Phys. Plasmas Fluids Relat. Interdiscip. Top.*, vol. 79, no. 2, 2009, Art. no. 026705.
[38] F. Tisseur, "Backward error and condition of polynomial eigenvalue problems," *Linear Algebra Appl.*, vol. 309, nos. 1–3, pp. 339–361, Apr. 2000.
[39] S. R. Seshadri, "Energy transport velocity of surface elastic waves," *J. Appl. Phys.*, vol. 54, no. 4, pp. 1699–1703, Apr. 1983.
[40] X. Su, Z. Lu, and A. N. Norris, "Elastic metasurfaces for splitting SV- and P-waves in elastic solids," *J. Appl. Phys.*, vol. 123, no. 9, Mar. 2018, Art. no. 091701.
[41] W. Zou, Z. He, and K. Hotate, "Two-dimensional finite-element modal analysis of Brillouin gain spectra in optical fibers," *IEEE Photon. Technol. Lett.*, vol. 18, no. 23, pp. 2487–2489, Dec. 1, 2006.
[42] C. Wolff, M. J. Steel, B. J. Eggleton, and C. G. Poulton, "Stimulated Brillouin scattering in integrated photonic waveguides: Forces, scattering mechanisms, and coupled-mode analysis," *Phys. Rev. A, Gen. Phys.*, vol. 92, no. 1, p. 013836, 2015.
[43] A. Gulistan, M. Rahman, S. Ghosh, and B. Rahman, "Elimination of spurious modes in full-vectorial finite element method based acoustic modal solution," *Opt. Exp.*, vol. 27, no. 8, pp. 10900–10911, 2019.
[44] S. Bramhavar, C. Prada, A. A. Maznev, A. G. Every, T. B. Norris, and T. W. Murray, "Negative refraction and focusing of elastic Lamb waves at an interface," *Phys. Rev. B, Condens. Matter*, vol. 83, no. 1, Jan. 2011, Art. no. 014106.
[45] T. Mensch and P. Rasolofosaon, "Elastic-wave velocities in anisotropic media of arbitrary symmetry-generalization of Thomsen's parameters ε, δ and γ," *Geophys. J. Int.*, vol. 128, no. 1, pp. 43–64, Jan. 1997.
[46] C. T. Sun and H. H. Huang, "Behavior of wave motion in an acoustic metamaterial with anisotropic mass density," in *IUTAM Symposium on Recent Advances of Acoustic Waves in Solids*. The Netherlands: Springer, 2010, pp. 149–163.

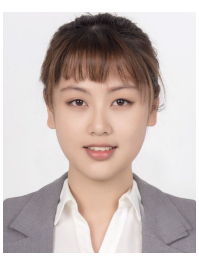

AN QI GE received the B.S. degree in mathematics and applied mathematics from Soochow University, Suzhou, China, in 2018. She is currently pursuing the Ph.D. degree with the School of Mathematical Sciences and the Institute of Electromagnetics and Acoustics, Xiamen University, Xiamen, China.

Her current research interests include spectral-element method for partial differential equation eigenvalue problems and numerical methods in elastic waves.

MING WEI ZHUANG (Member, IEEE) received the B.S. degree in applied physics from Shandong Jiaotong University, Jinan, China, in 2011, and the Ph.D. degree in radiophysics from the Institute of Electromagnetics and Acoustics, Xiamen University, Xiamen, China, in 2019.

From 2016 to 2017, he was a Visiting Student with the Department of Electrical and Computer Engineering, Duke University, Durham, NC, USA. His research interests include numerical methods in acoustic, viscoelastic, and poroelastic waves and imaging.

JIE LIU (Member, IEEE) received the B.S. degree in mathematics and applied mathematics and the M.S. degree in computational mathematics from Guizhou Normal University, Guiyang, China, in 2008 and 2012, respectively, and the Ph.D. degree in electromagnetic fields and microwave techniques from the Institute of Electromagnetics and Acoustics, Xiamen University, Xiamen, China, in 2019.

From July 2012 to July 2015, he was a Lecturer with the School of Mathematics and Statistics, Guizhou University of Finance and Economics, Guiyang. He is currently a Postdoctoral Researcher with the School of Informatics, Xiamen University. His current research interests include finite-element method and spectral-element method for partial differential equation eigenvalue problems and computational electromagnetics.

QING HUO LIU (Fellow, IEEE) received the B.S. and M.S. degrees in physics from Xiamen University, Xiamen, China, in 1983 and 1986, respectively, and the Ph.D. degree in electrical engineering from the University of Illinois at Urbana–Champaign, Champaign, IL, USA, in 1989.

He was a Research Assistant with the Electromagnetics Laboratory, University of Illinois at Urbana–Champaign, from September 1986 to December 1988, where he was a Postdoctoral Research Associate, from January 1989 to February 1990. He was a Research Scientist and the Program Leader of Schlumberger-Doll Research, Ridgefield, CT, USA, from 1990 to 1995. From 1996 to May 1999, he was an Associate Professor with New Mexico State University, Las Cruces, NM, USA. Since June 1999, he has been with Duke University, Durham, NC, USA, where he is currently a Professor of electrical and computer engineering. His research interests include computational electromagnetics and acoustics, inverse problems, and their application in nanophotonics, geophysics, biomedical imaging, and electronic design automation. He has published widely in these areas.

Dr. Liu is a fellow of the Acoustical Society of America, the Electromagnetics Academy, and the Optical Society of America. He received the 1996 Presidential Early Career Award for Scientists and Engineers (PECASE) from the White House, the 1996 Early Career Research Award from the Environmental Protection Agency, the 1997 Career Award from the National Science Foundation, the 2017 Technical Achievement Award and the 2018 Computational Electromagnetics Award from the Applied Computational Electromagnetics Society, and the 2018 Harrington-Mittra Award in Computational Electromagnetics from the IEEE Antennas and Propagation Society. In 2018, he also received the University of Illinois at Urbana–Champaign ECE Distinguished Alumni Award. He served as the founding Editor-in-Chief for the IEEE JOURNAL ON MULTISCALE AND MULTIPHYSICS COMPUTATIONAL TECHNIQUES. He has served as an IEEE Antennas and Propagation Society Distinguished Lecturer.